Graphene nanoribbon heterojunctions and heterostructures

Jinming Cai[1,2], Carlo A. Pignedoli[1], Leopold Talirz[1], Pascal Ruffieux[1], Hajo Söde[1], Liangbo Liang[3], Vincent Meunier[3], Reinhard Berger[4], Rongjin Li[4], Xinliang Feng[4], Klaus Müllen[4]*, Roman Fasel[1,5]*

1. Empa, Swiss Federal Laboratories for Materials Science and Technology, 8600 Dübendorf, Switzerland

2. Present address: Strategic Science International Limited, Hong Kong, China

3. Department of Physics, Rensselaer Polytechnic Institute, Troy, NY 12180, United States of America

4. Max Planck Institute for Polymer Research, 55124 Mainz, Germany

5. Department of Chemistry and Biochemistry, University of Bern, Freiestrasse 3, 3012 Bern, Switzerland

*e-mail: muellen@mpip-mainz.mpg.de, roman.fasel@empa.ch

Despite graphene's exciting properties[1,2], the lack of an electronic band gap severely limits its potential for applications in digital electronics[3,4]. In contrast, narrow stripes of graphene – so called graphene nanoribbons (GNRs) – are semiconductors due to quantum confinement[5,6], with a band gap that can be tuned by the nanoribbon width and edge structure[7-10]. Atomically precise GNRs can be obtained via a bottom-up approach based on the surface-assisted assembly of molecular precursors[11]. Here we report the fabrication of GNR heterojunctions and heterostructures by combining pristine hydrocarbon precursors with their nitrogen-substituted equivalents. Using scanning probe

methods, we show that the resulting heterostructures consist of seamlessly assembled segments of pristine (undoped) GNRs (p-GNRs) and deterministically nitrogen-doped GNRs (N-GNRs), which behave excitingly similar to traditional p-n-junctions[12]. With a band shift of 0.5 eV and an electric field of 2×10^8 V/m at the heterojunction, these materials bear high potential for applications in photovoltaics and electronics.

Figure 1a shows the pristine hydrocarbon precursor **1** that was previously used for the bottom-up fabrication of undoped, pristine GNRs (p-GNRs)[11]. For the fabrication of isostructural, but partially nitrogen doped GNRs (N-GNRs), the closely related precursor **2** (5,5'-(6,11-dibromo-1,4-diphenyltriphenylene-2,3-diyl)dipyrimidine) was synthesized (Supplementary Information S1, S2). Compared to **1**, two of the phenyl rings are replaced by pyrimidinyl rings in **2**, which results in a precursor exhibiting four nitrogen atoms at its periphery that are not expected to interfere in the polymerization and cyclodehydrogenation reactions towards N-GNRs as sketched in Fig. 1a. Precursor molecules **2** were sublimed under ultrahigh vacuum conditions onto a Au(111) surface held at a temperature of 200°C. They dehalogenate upon adsorption and colligate into linear polymer chains by radical addition (Supplementary Information S3). In a second thermal activation step at 400°C, surface-assisted cyclodehydrogenation establishes an extended, fully aromatic system. Its chevron topology ('nanowiggles'[13]) and the positions of the nitrogen atoms at the periphery are univocally defined by the design of the precursor **2**. The bottom-up method thus allows full control on dopant position and amount, unlike other methods reported for nitrogen-doping of graphene and related materials[14-16].

Figure 1b shows a scanning tunneling microscopy (STM) image of two adjacent Au(111) terraces covered with N-GNRs. Given that these N-GNRs are isostructural with the pristine, undoped GNRs (p-GNRs) obtained from **1**[11], it is not surprising that they cannot be distinguished from the latter in constant current STM images. Due to

the attractive N···H interaction between peripheral bipyrimidine units of neighboring N-GNRs, however, the packing of N-GNRs is strikingly different from the one of p-GNRs, thus providing an alternative means of distinguishing p- and N-GNRs. Figure 1c shows a small scale STM image overlaid with a model structure which clearly reveals the 'antiparallel' packing of N-GNRs. In fact, the ribbons are not exactly antiparallel to each other: a small shift along the ribbon axis is induced by the slightly interdigitating bipyrimidine units to stabilize the antiparallel packing. The attractive interaction between N-GNRs leads to aggregation of ribbons according to Fig. 1c even at low coverage, whereas p-GNRs tend to repel each other and to orient along the Au(111) surface reconstruction at low coverage[11].

Since p- and N-GNRs obtained from **1** and **2**, respectively, have identical geometrical but different electronic structures, heterojunctions and heterostructures can be formed via sequential GNR build up from the corresponding precursors. Figure 2a shows an example of a p-N-GNR heterostructure containing alternating short segments of p-GNRs (grey) and N-GNRs (blue). To realize such heterostructures, precursors **1** and **2** were alternatingly deposited on a Au(111) substrate kept at 200°C to induce copolymerization. The sample with the resulting "diblock copolymer" strands was subsequently annealed to 420 °C for cyclodehydrogenation. The STM image of a sample fabricated accordingly (Fig. 2b) reveals ribbons exhibiting the expected chevron topology. A discrimination of the two kinds of GNR segments in the heterostructures is difficult. A first indication can be obtained from their tendency to assemble with antiparallel alignment (N-GNR) or to stay away from each other (p-

GNR). Due to the different electronic structure of the N-GNR segments, however, electronic property measurements reveal more details within these heterostructures. For the heterostructures shown in Fig. 2c, we performed differential conductance dI/dV measurements (Fig. 2d & e)[17] . The two dI/dV maps recorded at -0.35 V and -1.65 V exhibit a clear contrast inversion that allows discrimination of two different types of GNR segments. Considering that only N-GNRs pack in a slightly shifted antiparallel configuration, the ribbon segments entering the scan window from the bottom left can be identified as N-GNRs. Both pieces of information then yield the picture displayed in Fig. 2f, where N-GNR and p-GNR segments are artificially highlighted in blue and light grey, respectively.

To shed light on the electronic properties of the chevron N-GNRs we have performed density functional theory (DFT) calculations for both p- and N-GNRs. Band structures for infinitely long (periodic) p- and N-GNR are presented in Fig. 3b & d, respectively. Both ribbons have similar DFT gaps (1.6 eV and 1.5 eV for p- and N-GNR, respectively), but there is a sizeable offset of the bands: The valence band maximum (VBM) of the N-GNR is 0.6 eV lower in energy than the VBM of the p-GNR; a similar shift of 0.7 eV applies to the conduction band minimum (CBM), in line with predicted n-type transistor behavior for nitrogen doped GNRs[18-21]. To confirm this picture experimentally, both GNRs were synthesized one after the other on the same Au(111) substrate, and STM differential conductance (dI/dV) maps of a region with both p- and N-GNRs were taken (Supplementary Information S4): both GNRs have similar band gaps of ~2.0 eV on Au(111), and the CBM and VBM of the N-GNR are

indeed shifted to lower energies by as much as ~1.1 eV (Supplementary Information S4), in qualitative agreement with calculations. We further note that the pristine p-GNRs are indeed "p-doped" due to the interaction with the underlying Au(111) surface, as evidenced by the location of the VBM close to the Fermi level of the metal substrate (Fig. S5).

The observed energy offset of CBM and VBM from p-GNRs to N-GNRs raises the interesting question how the electronic bands will align in p-N-GNR heterostructures. In principle, seamlessly fused p- and N-GNR segments as shown in Fig. 2 should result in type-II staggered gap heterojunctions which are of considerable interest for photovoltaic and electronic applications[22,23]. In a first step, we have employed DFT to compute the electronic properties of a realistic heterojunction of 20 nm length, containing more than 1200 atoms. Figure 3a provides a chemical sketch of the corresponding interface between the p-GNR (gray) and N-GNR (blue). The computed densities of states projected (PDOS) on the p-GNR and on the N-GNR segment regions far from the junction are given in Fig. 3c in gray and blue, respectively. Both the VBM and CBM reveal significant downshifts of 0.45 eV and 0.55 eV, respectively, from the p-GNR segment to the N-GNR segment, demonstrating that the p-N-GNR junction indeed leads to a staggered gap configuration. To further characterize the interface region where the band shift occurs we plot in Fig. 3e the local densities of states (LDOS), averaged in a plane perpendicular to the ribbon axis, across the p-N-GNR junction (Fig. 3f). The LDOS map reveals that the interface is extremely sharp – band bending occurs over a distance of the order of 2 nm. Both the

valence bands (VB) and the conduction bands (CB) have thus reached their 'bulk' energy positions already one monomer unit away from the heterojunction. The band offset of about 0.5 eV – which is as large as the one of GaAs/$Al_xGa_{1-x}As$ or AlN/GaN heterojunctions[24] – and the narrow interface region over which the band shift occurs, should result in a significant electrostatic field at the interface. Figure 3g demonstrates the change in electrostatic potential across the interface region. From its slope at the interface we derive an electric field of 2×10^8 V/m, which is at least two orders of magnitude higher than in traditional semiconductor p-n junctions where the width of the depletion region is the limiting factor[23]. Correspondingly high charge carrier separation efficiency may thus be expected for p-N-GNR heterojunctions what makes them highly promising for photovoltaics, but also for the wide range of electronic device components based on p-n junctions[23].

The band bending across the p-N-GNR heterojunction occurs within only 2 nm (Fig. 3 e, see also Supplementary Information S8), and should thus be observable even for heterostructures consisting of very short p- and N-GNR segments (one to a few monomer units). We experimentally explored this extreme situation by fabricating heterostructures via rapidly alternating precursor deposition. An example of the resulting p-N-GNR heterostructures is presented in Fig. 4. Using STM differential conductance dI/dV measurements taken at different energies between -1.8 eV and +1.8 eV we determined the band shifts in short segment heterostructures. From the appearance/disappearance of differential conductance – and thus LDOS – we derived the energy positions of VBM and CBM. Figure 4 c-f displays the dI/dV maps taken

around the identified energy positions of the CBM for the p- and N-GNR segments (red/white star and triangle symbols in Fig. 3) with the corresponding data for the VBM given in the Supplementary Information (S5).

At 1.35 eV, high differential conductance (violet) – and thus high LDOS – is observed in all segments (Fig. 4c). At this energy, we are therefore well within the CB for both the p- and N-GNR segments. Moving down in energy to 1.15 eV (Fig. 4d), intensity disappears on some of the GNR segments, which identifies them as p-GNR segments since the bias energy is located in the band gap, below the CBM. The intensity on the N-GNR segments remains essentially unchanged down to energies of 0.85 eV (Fig. 4e), but disappears at 0.65 eV (Fig. 4f), where the bias has entered into the band gap of the N-GNR segments. We thus infer the energy positions of the CBM of p-GNR and N-GNR segments at ~1.25 eV and ~0.75 eV, respectively, corresponding to a CB offset of ~0.5 eV in agreement with the calculations discussed above. From the corresponding data on the VB region (Supplementary Information S5) we derive VBM positions of ~-0.75 eV and -~1.25 eV for p- and N-GNR segments, respectively, and thus a VB offset of ~0.5 eV. These data clearly confirm the theoretical picture (Fig. 3) of staggered gap heterojunctions with a band offset of ~0.5 eV. Figure S5 of the Supplementary Information summarizes the band edge positions and offsets derived from dI/dV maps for p- and N-GNRs and the p-N-heterojunctions discussed here above. Complementary DFT simulations of the DOS, electrical conductance and LDOS plots for p-N-GNR heterojunction are shown in Fig. S6 & S7 and are in good agreement with the experimental findings, clearly highlighting the

essential band offset phenomena and the fundamental difference between electronic and transport gaps in type II heterojunctions.

The observed band offset across p-N-GNR heterojunctions arises from the more attractive core potential of the nitrogen dopants. Higher/lower nitrogen doping levels in confined positions are thus expected to lead to larger/smaller band shifts. A smaller shift of about 0.27 eV – roughly one half of the one observed here – has indeed been reported for chevron GNRs substituted with two nitrogen atoms per monomer unit[25] – which corresponds to one half the substitution level used here. This suggests that nitrogen incorporation in precursor monomers results in GNRs with bands shifted down in energy by about 0.13 eV per nitrogen atom. Doping levels from 1 to 6, or even 8, nitrogens per monomer are readily conceivable (Supplementary Information S9), with concomitant band shifts of 0.13 eV up to 1 eV. This strategy thus opens a new route for highly-controlled (at the atomic level) doping schemes providing exquisite control of energy levels, in departure from existing technologies. Together with the wide tunability of the band gap via the nanoribbon width, p-N-GNR heterostructures thus offer the unique opportunity of heterojunction engineering with respect to both, the band gap and the band offset.

In view of technological applications, obvious requirements are the scalability of the GNR heterostructure fabrication process and the use of non-conductive substrates. To this end, we have developed an efficient GNR fabrication procedure based on Au-on-mica substrates, and a clean and reliable transfer method for bringing the fabricated

GNRs onto arbitrary target substrates (Supplementary Information S10). Based on similar procedures, the realization of GNR field-effect transistors has recently been demonstrated[26]. Further studies along the materials development path toward future electronic devices are in progress, and we expect p-N-GNR heterostructures to become extremely versatile components for applications in photovoltaics and electronics.

Methods

Sample preparation and STM measurements. Au(111) single crystals (Surface Preparation Laboratory, Netherlands) were used as substrates for GNR growth. All experiments were performed under ultrahigh vacuum conditions. Substrate surfaces were cleaned by repeated cycles of argon ion bombardment and annealing to 470 °C. Precursor monomers (for details on the synthesis, see the Supplementary Information S1) were deposited onto the clean substrate surfaces by sublimation at rates of ~ 2 Å/min. For the fabrication of N-GNRs, the substrate was maintained at 200 °C during monomer deposition to induce dehalogenation and radical addition. After deposition, the sample was post-annealed at 400 °C for 10 min to cyclodehydrogenate the polymers and form GNRs. For the p-GNRs, the preparation process was identical, except that slightly higher substrate temperatures of 250 °C and 440 °C were used during monomer deposition and for post-annealing, respectively. For the fabrication of heterostructures, the two precursor species were evaporated one after the other for several cycles on a Au(111) surface held at 200 °C, which was subsequently annealed to 420 °C. A variable temperature scanning tunneling microscope (VT-STM, Omicron Nanotechnology GmbH, Germany) operated with liquid Helium cooling (sample temperature ~35 K) was used for observing the morphology of GNRs in the constant current mode under ultra-high vacuum conditions (<5e-11 mbar). Differential conductance dI/dV measurements were performed in a low temperature STM (LT-STM, Omicron Nanotechnology GmbH, Germany) operated at 5 K using a standard lock-in technique with modulation frequency of 860 Hz and root-mean

squared amplitude of 20 mV.

Calculation methods. Atomistic simulations were performed within the framework of density functional theory. We have employed norm-conserving pseudopotentials of the Goedecker-type[27] and the PBE[28] approximation to the exchange correlation functional. Band structures were calculated with the Quantum Espresso package[29], using a simulation cell with a lattice parameter of 17.1 Å, containing 108 (100) atoms for the p-GNR (N-GNR). More than 20 Å of vacuum in the other two directions were included in order to decouple periodic images. The reciprocal space was sampled by 28 k-points. A large-scale model of a finite p-N-GNR heterojunction was treated within the mixed Gaussian plane wave approach implemented in the CP2K code[30]. The simulation cell contained 1270 atoms (GNR length ~210 Å) and more than 20 Å of vacuum in each direction.

Acknowledgement

This work was supported by the Swiss National Science Foundation, by the State Secretariat for Education, Research and Innovation via the COST Action MP0901 "NanoTP", by the European Science Foundation under the EUROCORES Program EuroGRAPHENE (GOSPEL), ERC NANOGRAPH, EU GENIUS project, Graphene Flagship and by the Office of Naval Research BRC Program. The authors would like to acknowledge discussions with Daniele Passerone. J.C. thanks Roland Widmer, Jia Liu and Carlos Sánchez Sánchez for help with the experiments.

Author Contributions

J.C., P.R, R.F., X.F. and K.M. conceived and designed the experiments. R.B. synthesized the molecular precursors. J.C. performed the growth and scanning probe experiments. J.C. and H.S. did the scanning tunneling spectroscopy analysis. R.L. and X.F. developed the transfer process and performed the Raman measurements. C.A.P., L.T., D.P., L.L. and V.M. performed the simulations. J.C. and R.F. prepared the figures and wrote the paper. All authors discussed the results and implications and commented on the manuscript.

Additional information

Supplementary information is available in the online version of the paper. Reprints and permissions information is available online at www.nature.com/reprints. Correspondence and requests for materials should be addressed to R.F.

1. Morzov, S.V. *et al*. Giant intrinsic carrier mobilities in graphene and its bilayer. *Phys. Rev. Lett.* **100**, 016602, (2008).

2. Novoselov, K.S. *et al*. Electric field effect in atomically thin carbon films. *Science* **306,** 666-669 (2004).

3. Castro Neto, A. H., Guinea, F., Peres, N. M. R., Novoselov, K. S. & Geim, A. K. The electronic properties of graphene. *Rev. Mod. Phys.* **81**, 109-162 (2009).

4. Kotov,V. N., Uchoa, B., Pereira, V. M., Guinea, F. & Castro Neto, A. H. Electron-electron interactions in graphene: current status and perspectives, *Rev. Mod. Phys.* **84,** 1067-1125 (2012)

5. Wakabayashi, K. Electronic transport properties of nanographite ribbon junctions. *Phys. Rev. B* **64,** 125428 (2001).

6. Barone, V., Hod, O. & Scuseria, G. E. Electronic structure and stability of semiconducting graphene nanoribbons. *Nano Lett.* **6,** 2748-2754 (2006).

7. Chen,Y., Oteyza, D., Pedramrazi, Z., Chen, C., Fischer, R. F. & Crommie, F. M. Tuning the band gap of graphene nanoribbons synthesized from molecular precursors, *Acs Nano* **7,** 6123-6128 (2013).

8. Son, Y.W., Cohen, M.L. & Louie, S.G. Half-metallic graphene nanoribbons. *Nature* **444,** 347-349 (2006).

9. Yang, L. *et al.* Quasiparticle energies and band gaps in graphene nanoribbons. *Phys. Rev. Lett.* **99,** 186801 (2007).

10. Ruffieux, P. *et al.* Electronic structure of atomically precise graphene nanoribbons. *ACS Nano* **6**, 6930–6935 (2012).

11. Cai, J. *et al.* Atomically precise bottom-up fabrication of graphene nanoribbons. *Nature* **466,** 470-473 (2010).

12. Kittel, C. *Introduction to Solid State Physics, 5th Edition* (Wiley, New York, 1976).

13. Girao E. C., Liang, L., Cruz-Silva E., Souza Filho A. G. and Meunier, V. Emergence of atypical properties in assembled graphene nanoribbons. *Phys. Rev. Lett.* **107,** 135501 (2011).

14. Wang, X.R., *et al.* N-doping of graphene through electrothermal reactions with ammonia. *Science*, **324**, 768-771 (2009).

15. Panchakarla, L.S. *et al.* Synthesis, structure, and properties of boron- and nitrogen-doped graphene. *Adv. Mater.* **21**, 4726-4730 (2009).

16. Wei, D.C. *et al.* Synthesis of N-doped graphene by chemical vapor deposition and its electrical properties. *Nano Lett.* **9,** 1752-1758 (2009).

17. Braun, K.F. & Rieder, K.H. Engineering electronic lifetimes in artificial atomic structures. *Phys. Rev. Lett.* **88,** 096801 (2002).

18. Yan, Q.M. *et al.* Intrinsic current-voltage characteristics of graphene nanoribbon transistors and effect of edge doping. *Nano Lett.* **7**, 1469-1473 (2007).

19. Li, Y.F. *et al.* Spin gapless semiconductor-metal-half-metal properties in nitrogen-doped zigzag graphene nanoribbons. *Acs Nano* **3,** 1952-1958 (2009).

20. Boukhvalov, D.W. & M.I. Katsnelson, Chemical Functionalization of Graphene with Defects. *Nano Lett.* **8,** 4373-4379 (2008).

21. Yu, S.S. et al. First principle calculations of the electronic properties of nitrogen-doped carbon nanoribbons with zigzag edges. *Carbon* **46,** 537-543 (2008).

22. Cocchi, C., Ruini, A., Prezzi, D., Caldas, M. J. & Molinari, E. Designing all-graphene nanojunctions by covalent functionalization. *J Phys Chem C* **115,** 2969–2973 (2011).

23. Neamen, D. A. *Semiconductor Physics and Devices: Basic Principles*, *3rd Edition* (McGraw-Hill, Boston, 2003).

24. Nag, B.R. *Physics of Quantum Well Devices* (Springer, Berlin, 2000)

25. Bronner, C. *et al.* Aligning the band gap of graphene nanoribbons by monomer doping. *Angew.*

Chem. Int. Edn Engl. **52,** 4422-4425 (2013).

26. Bennett, P. B. *et al*., Bottom-up graphene nanoribbon field-effect transistors. *Appl. Phys. Lett.* **103**, 253114 (2013).

27. Goedecker, S., Teter, M. & Hutter, J. Separable dual-space Gaussian pseudopotentials. *Phys. Rev. B* **54,** 1703–1710 (1996).

28. Perdew, J. P., Burke, K. & Wang, Y. Generalized gradient approximation for the exchange-correlation hole of a many-electron system. *Phys. Rev. B* 54, 16533–16539 (1996)

29. Giannozzi, P. *et al.* Quantum espresso: a modular and open-source software project for quantum simulations of materials. *J. Phys.: Condens. Matter* **21,** 395502 (2009).

30. VandeVondele, J. *et al.* Fast and accurate density functional calculations using a mixed Gaussian and plane waves approach. *Comput. Phys. Commun.* ***167*****,** 103–128 (2005).

Figure legends

Figure 1 | **Bottom-up fabrication of N-GNRs. a**, A slight variation of monomer **1** (6,11-dibromo-1,2,3,4-tetraphenyltriphenylene) previously used for the fabrication of pristine chevron-type armchair GNRs[11] yields the nitrogen-substituted monomer **2** (5,5'-(6,11-dibromo-1,4-diphenyltriphenylene-2,3-diyl)dipyrimidine) that allows for the fabrication of N-GNRs in two steps: formation of linear polymers by covalent interlinking of the dehalogenated intermediates, and formation of fully aromatic N-GNRs by cyclodehydrogenation. **b**, Overview STM image of N-GNRs on Au(111) (T=35 K, U=1.0 V, I=0.1nA). **c**, Small-scale STM image with partly overlaid structural model of the ribbons revealing their specific alignment due to N-H interactions (T=35 K, U=-1.3 V, I=0.3 nA).

Figure 2 | **Fabrication and identification of p-N-GNR heterojuctions. a**, Chemical structure of a nanoribbon combining segments of p-GNRs (gray) and N-GNRs (blue). **b**, Overview STM image of p-N-GNR heterostructures on Au (111) (T=35 K, U=2.0 V, I=0.03nA). **c**, Small scale STM image of p-N-GNR heterostructures **(**T=5 K, U=-0.35 V, I=0.15nA), and **d & e,** the corresponding differential conductance dI/dV maps (T=5 K, I=0.15nA, V_{mod}=20mV, ν=860 Hz) taken at bias voltages of U=-0.35 V (**d**) and -1.65 V (**e**), respectively. The contrast inversion (violet/green) between **d** and **e** allows a clear distinction of the two chemically different ribbon segments. In **f**, the identified p-GNR and N-GNR segments are highlighted in gray and blue, respectively.

Figure 3 | Band offset across p-N-GNR heterojunctions. a, Sketch of a heterojunction between a p-GNR segment (left part, grey) and a N-GNR segment (right part, blue). **b & d,** Computed band structures of a p-GNR (**b**) and a N-GNR (**d**), both aligned to the Hartree potential in vacuum (i.e. energies are given with respect to the vacuum level). **c**, PDOS of the p-GNR segment (left, gray) and the N-GNR segment (right, blue) of the heterojunction shown in (**a**). The p-N-GNR heterojunction exhibits a staggered gap configuration with band offsets of 0.45 eV (valence band) and 0.55 eV (conduction band). Red symbols refer to energy positions of dI/dV maps shown in Figures 4 and S4 (Supplementary Information). **e**, The LDOS across the heterojunction shown in (**f)** reveals a very narrow interface region of ~2 nm over which the band offset of ~0.5 eV occurs. This results in a high electric field of the order of 2×10^8 V/m, as derived from the gradient of the potential across the heterojunction shown in (**g**).

Figure 4 | Differential conductance d*I*/d*V* maps of p-N-GNR heterostructures. As a guide to the eye, heterostructures are outlined by white dashed lines in all panels. **a & b**, STM image (T=5K, U=1.35 V, I=0.15 nA) of p-N-GNR heterostructures. In (**b**), the p- and N-GNR units are indicated by gray and blue dots, respectively. **c-f**, Representative selection of dI/dV maps taken in the conduction band region (T=5K, ν=860 Hz, U_{mod}=20mV), at energy positions around the conduction band minimum. Red symbols relate these energy positions to the evolution of the conduction band minimum across a heterojunction, as shown in Fig. 3.

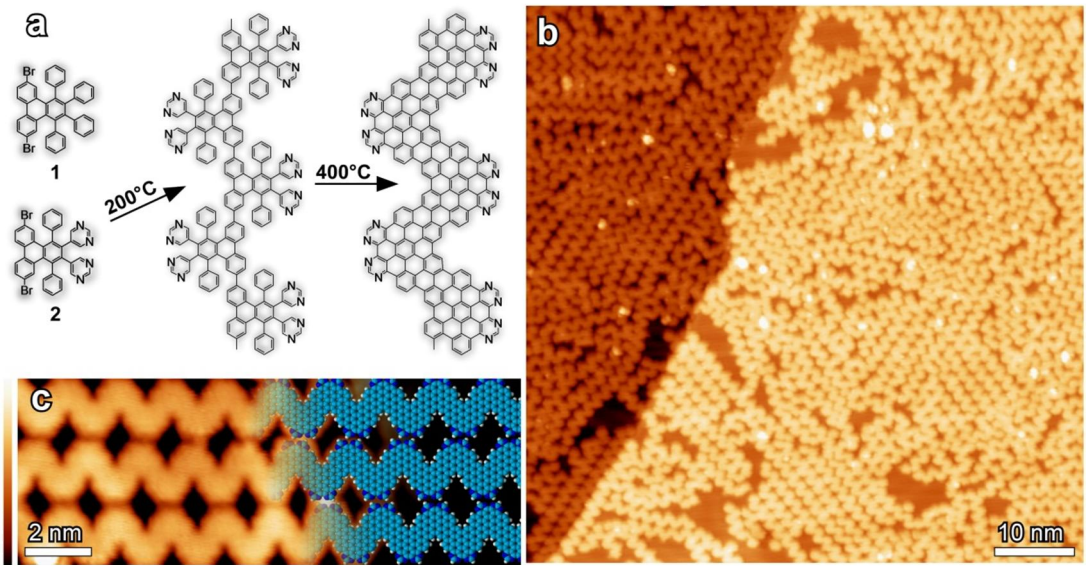

Figure 1

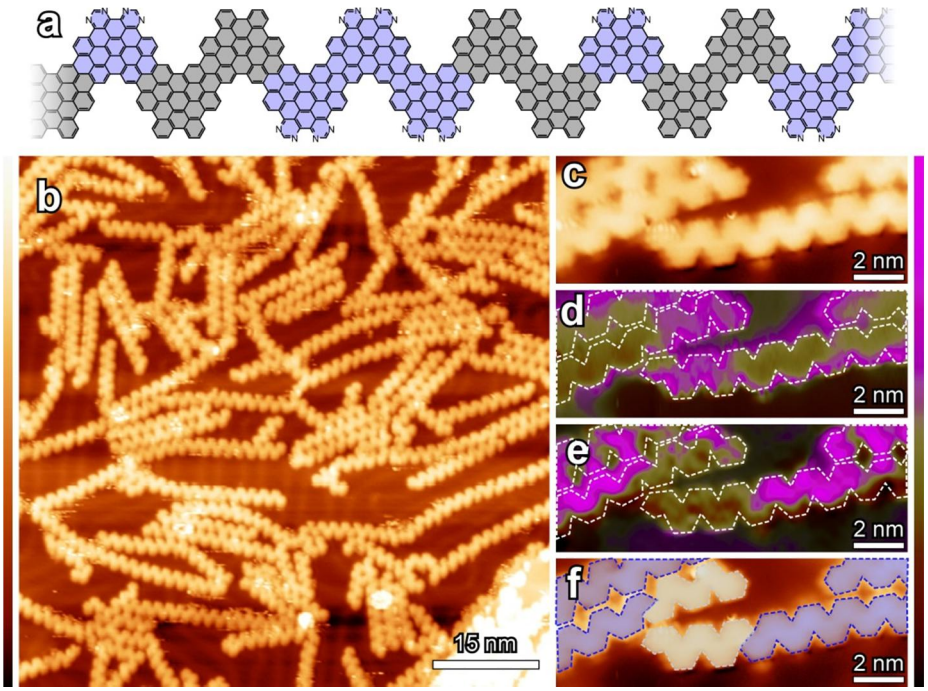

Figure 2

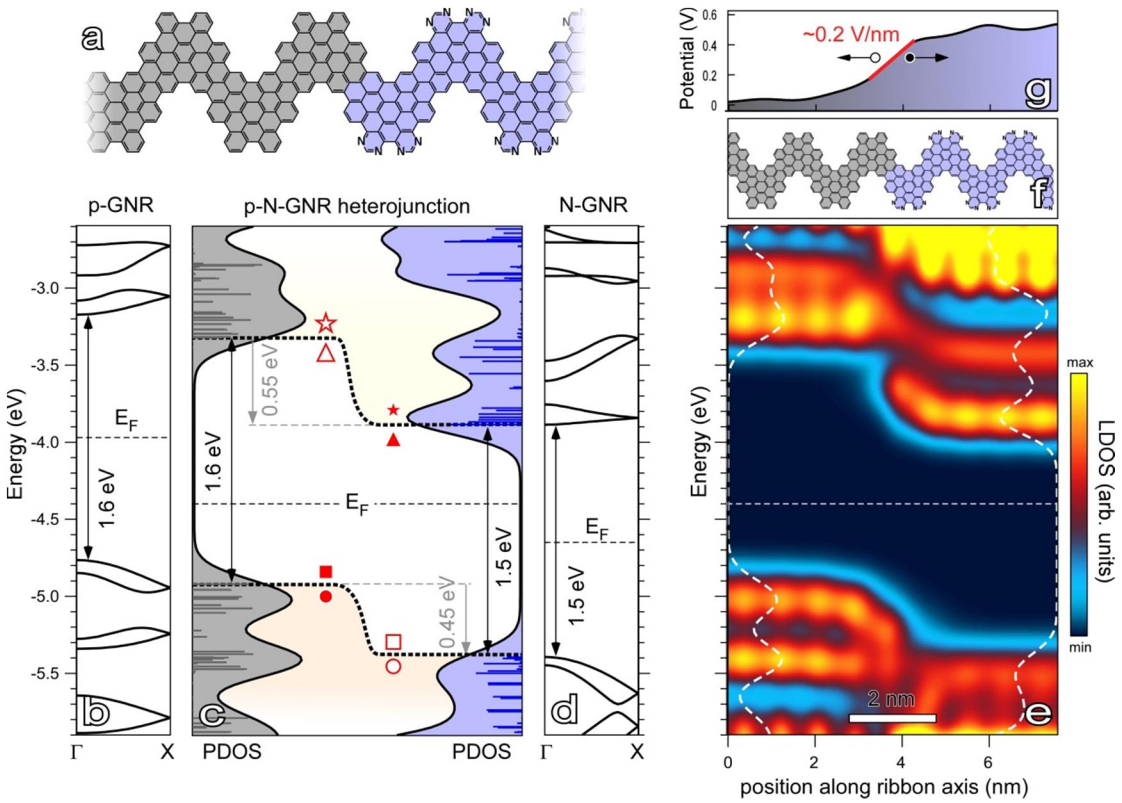

Figure 3

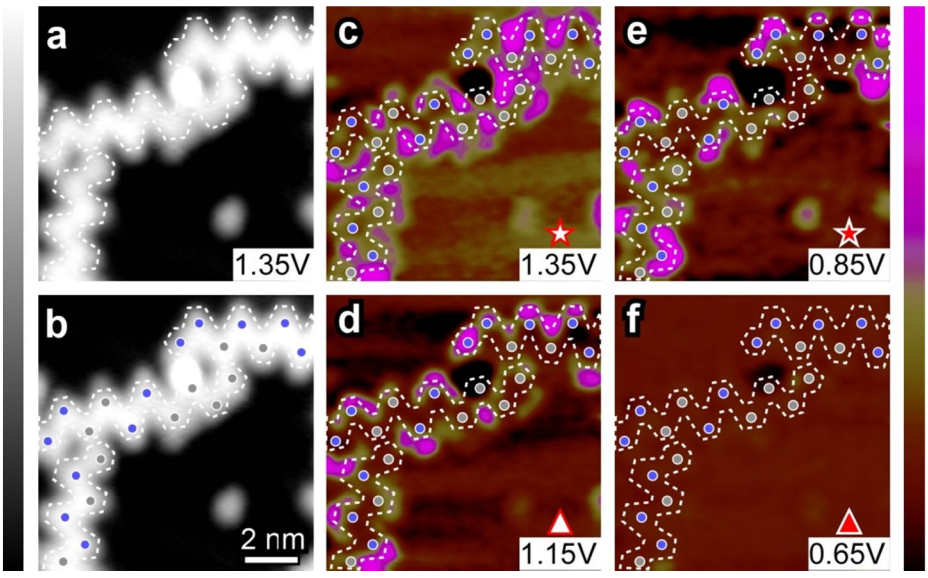

Figure 4